CrossMark

# Thermoelectric Properties of Nb-Doped SrTiO$_3$/TiO$_2$ Eutectic Solids Fabricated by Unidirectional Solidification

YUUI YOKOTA [1,7] SHIGERU HORII,[2] HIRAKU OGINO,[3]
MASAO YOSHINO,[4] AKIHIRO YAMAJI,[4] YUJI OHASHI,[1]
SHUNSUKE KUROSAWA,[1,5] KEI KAMADA,[1,6]
and AKIRA YOSHIKAWA[1,4,6]

1.—New Industry Creation Hatchery Center (NICHe), Tohoku University, 6-6-10, Aoba, Aramaki, Aoba-ku, Sendai, Miyagi 980-8579, Japan. 2.—Graduate School of Energy Science, Kyoto University, Yoshida-Honmachi, Sakyo-ku, Kyoto 606-8501, Japan. 3.—National Institute of Advanced Industrial Science and Technology (AIST), 1-1-1 Central 2, Umezono, Tsukuba, Ibaraki 305-8568, Japan. 4.—Institute for Materials Research, Tohoku University, 2-1-1, Katahira, Aoba-ku, Sendai, Miyagi 980-8577, Japan. 5.—Department of Physics, Yamagata University, Kojirakawa-mach 1-4-12, Yamagata 990-8560, Japan. 6.—C&A Corporation, 6-6-40, Aoba, Aramaki, Aoba-ku, Sendai, Miyagi 980-8579, Japan. 7.—e-mail: yokota@imr.tohoku.ac.jp

Undoped and Nb-doped SrTiO$_3$/TiO$_2$ (STO/TO) eutectic solids were fabricated from the melt at a eutectic point of STO and TO by unidirectional solidification. Fabricated undoped and Nb:STO/TO eutectic solids were composed of the TiO$_2$ rod-like and the SrTiO$_3$ matrix phases, and the periodic and uniform eutectic morphology could be achieved in the Nb:STO/TO eutectic solids by stable control of the liquid–solid interface during the fabrication. The thermal conductivity of the Nb:STO/TO eutectic solid was less than half of that of the Nb:STO single crystal owing to the decrease of the lattice thermal conductivity by phonon scattering at the grain boundaries. The figures of merit $ZT$'s of the Nb:STO/TO eutectic solid, parallel and perpendicular to the growth direction, were $\sim 0.007$ and $\sim 0.0004$, respectively. The small $ZT$'s are attributable to the higher electrical resistivity originating from the insufficient carrier doping and high electrical resistivity of the TO phase.

**Key words:** Thermoelectric material, eutectic material, SrTiO$_3$, TiO$_2$, unidirectional solidification

## INTRODUCTION

A eutectic material with a phase-separated structure (eutectic structure) composed of a rod phase in a matrix phase or a lamella configuration can be fabricated by unidirectional solidification from the melt with the chemical composition at a eutectic point.[1–10] Functional eutectic materials with the eutectic morphology have been investigated as materials with high mechanical strength, as a scintillator with an optical waveguide structure, and as an optical material.[2–8] The Ce:GdAlO$_3$/Al$_2$O$_3$ eutectic scintillator achieved high-resolution x-ray imaging as a result of the phase-separated configuration with the rod phase of Ce:GdAlO$_3$ scintillator in the $\alpha$-Al$_2$O$_3$ matrix phase.[6] In addition, a Ce:Y$_3$Al$_5$O$_{12}$/Al$_2$O$_3$ eutectic solid grown by the vertical Bridgman method has been developed for the application to white-light-emitting diodes.[9,10]

There are many studies of thermoelectric materials that were fabricated using nanopowders and included impurity nanopowders to improve their figure of merit ($ZT$) by decreasing the thermal conductivity originating from the phonon scattering at the grain boundaries.[11–15] For example, bulk Nb-doped SrTiO$_3$ (Nb:STO) composed of nanopowders showed a lower thermal conductivity [5.0 W/(m K)] than Nb:STO single crystal [10 W/(m K) at

300 K].[11] In addition, the thermal conductivity of a Nb:STO sample including yttria-stabilized zirconia (YSZ) nanoparticles reached 4.3 W/(m K) at 300 K.[12] Moreover, there are some previous studies of eutectic materials fabricated from the melt.[16,17] Eutectic morphology of particle-like $MnTe_2$ and lamellar MnTe precipitates was spontaneously formed in $Pb_{1-z}Mn_zTe$, and the disconnected particle-like precipitates effectively reduced the lattice thermal conductivity.[17] However, in the previous studies of thermoelectric eutectic materials, the eutectic morphologies were not controlled by unidirectional solidification, and they were not composed of a uniform phase-separated configuration.

On the basis of this background, we developed a phase-separated thermoelectric material by unidirectional solidification to achieve a periodic and uniform eutectic morphology in a bulk composite and reveal the effects of eutectic morphology on the thermoelectric properties. If the phase-separated eutectic material has the periodic and uniform eutectic morphology composed of a scattering phase in a matrix phase of a thermoelectric material, the eutectic morphology can decrease the thermal conductivity as in the case of the Nb:STO bulk composed of nanopowder and the Nb:STO including YSZ nanoparticles. In this study, the eutectic material including the STO with high Seebeck coefficient and thermal conductivity[18] was selected for the first trial of a thermoelectric eutectic material fabricated by unidirectional solidification.

Figure 1 is a $SrO-TiO_2$ phase diagram[19] and the STO phase appears at the chemical composition of $SrO:TiO_2 = 50:50$. There is a eutectic point of STO and $TiO_2$ (TO) phases at the chemical composition of $SrO:TiO_2 = 20:80$. Composite at the eutectic point is composed of 40 mol.% STO and 60 mol.% TO (40%STO/60%TO), and the melting point is 1440°C. Therefore, we developed undoped and Nb-doped 40%STO/60%TO eutectic solids from the melt by unidirectional solidification, and investigated the microstructures, phases, chemical compositions, and thermoelectric properties in this study.

## EXPERIMENTAL

Eutectic solids with the chemical composition of 40%STO/60%TO were fabricated by a micro-pulling-down ($\mu$-PD) method that could grow functional single crystals and metal fibers from the melt using a crucible.[20–24] Starting materials, $SrCO_3$, $TiO_2$, and $Nb_2O_5$ powders ($> 4$ N), were mixed as nominal compositions at the eutectic point of STO and TO, $(Sr_{1-x}Nb_x)TiO_{3+\delta}$: $TiO_2 = 40: 60$ ($x = 0$ and 0.2). The mixed powder was sintered at 1200°C for 12 h in air, and the sintered powder was set in an iridium crucible with a die at the bottom. There are five holes in the die that can pass the melt in the crucible to the bottom. The crucible was set in the center of a radio-frequency (RF) induction coil, and it was surrounded by alumina insulators in the $\mu$-
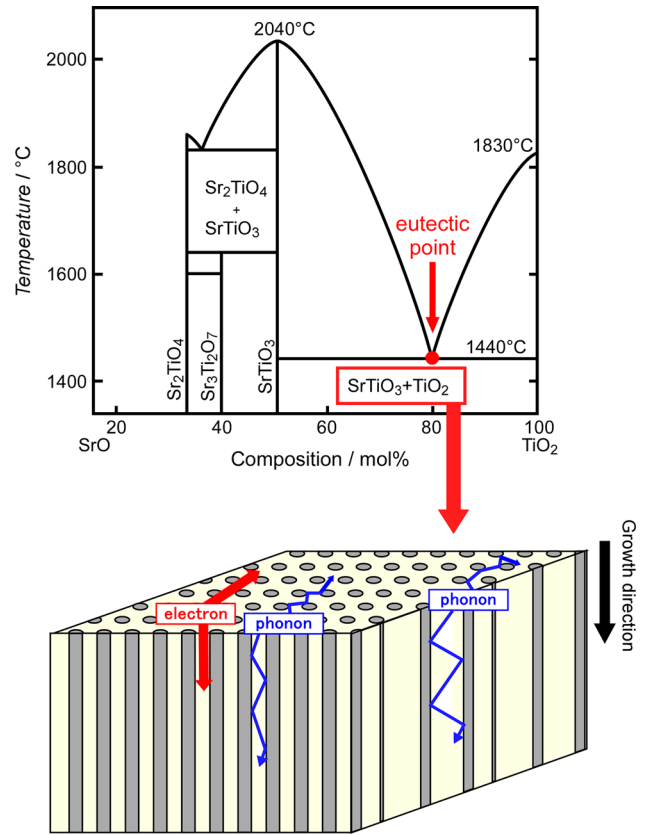


Fig. 1. The phase diagram of $SrO-TiO_2$ and a schematic diagram of a eutectic solid fabricated by unidirectional solidification.

PD furnace produced by TDK. The crucible was heated up to the melting point of the STO/TO (1440°C) in $N_2$ by the RF induction coil. After the sintered powder in the crucible was completely melted, undoped and Nb-doped STO/TO eutectic solids were fabricated by pulling down the melt using an $Al_2O_3$ ceramic rod as a seed. Pulling-down was controlled by a driving motor. After the growth of eutectic solids, the fabricated fibers were cooled to room temperature. The fabricated eutectic solids were cut parallel and perpendicular to the growth direction, and specimens were polished for observations of microstructure and measurements of thermoelectric properties.

Powder x-ray diffraction measurement was performed to identify the phases of the eutectic solids after they were ground by an agate mortar. The microstructure on the polished surface of the eutectic solids was observed by a scanning electron microscope (SEM) using the back-scattering electron (BSE) mode. The chemical composition of each phase in the BSE images was analyzed by energy dispersive x-ray spectrometry (EDX). The thermoelectric properties (thermal conductivity, Seebeck coefficient, and electrical resistivity) were evaluated in the temperature range of 5–300 K by a Physical Property Measurement System (PPMS®). Two specimens were prepared from the fabricated Nb:STO/
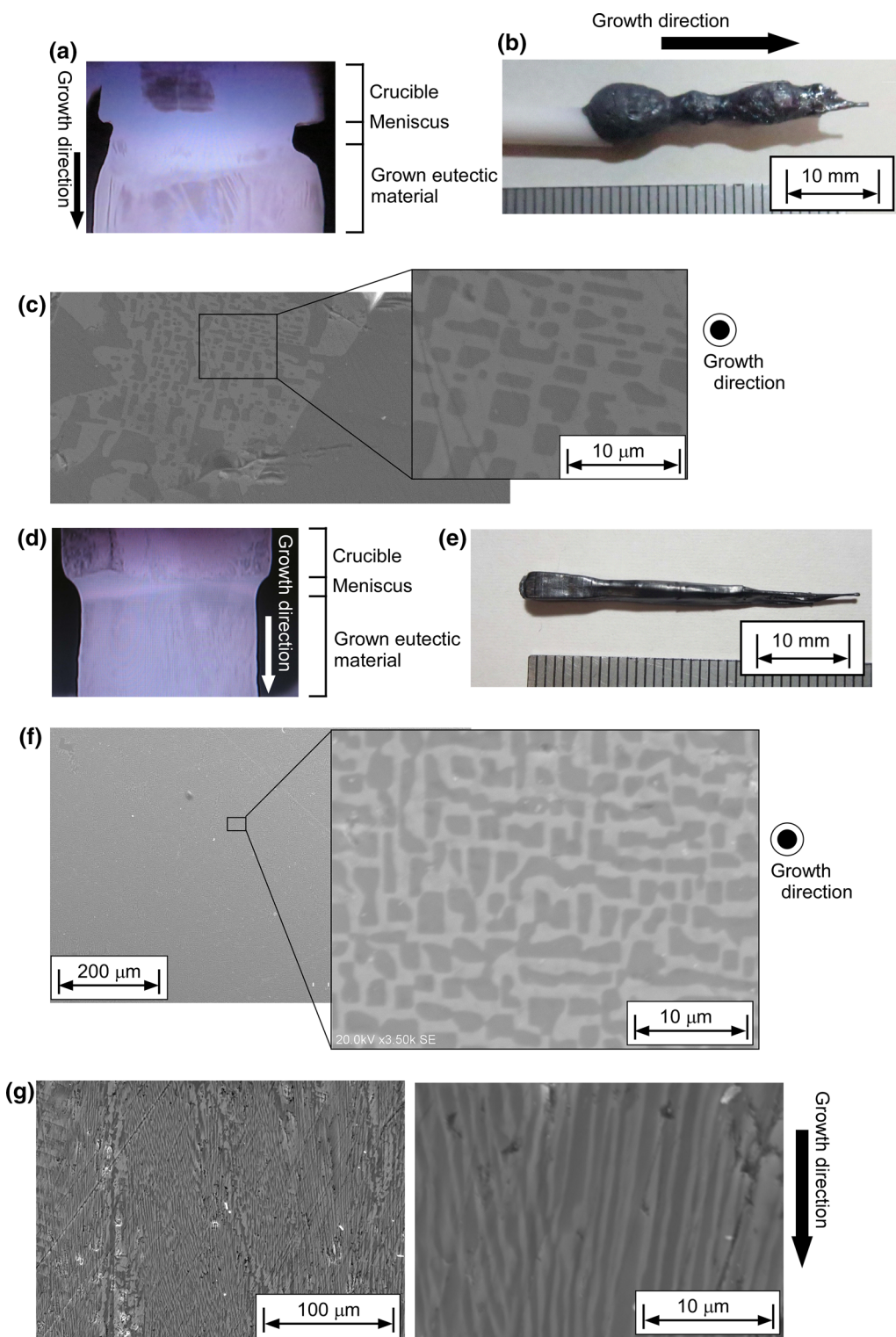
Fig. 2. (a) Liquid–solid interface during the fabrication of the undoped STO/TO eutectic solid. (b) Undoped STO/TO eutectic solid and (c) BSE image perpendicular to the growth direction. (d) Liquid–solid interface during fabrication of the Nb:TO/TO eutectic solid. (e) Nb:STO/TO eutectic solid and (f, g) BSE images perpendicular and parallel to the growth direction.
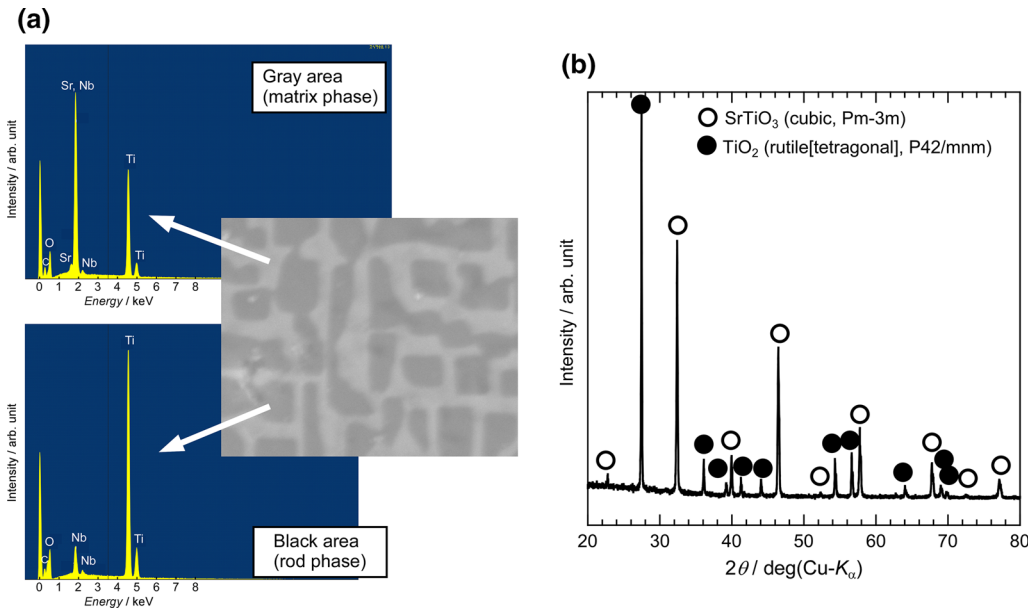
Fig. 3. (a) EDX spectra and (b) XRD pattern of the Nb:STO/TO eutectic solid.

TO eutectic solid for the measurements of thermo-electric properties parallel and perpendicular to the growth direction.

## RESULTS AND DISCUSSION

Undoped and Nb-doped STO/TO eutectic solids were fabricated by the $\mu$-PD method using the Ir crucible. The liquid–solid interface during fabrication of the undoped STO/TO eutectic solid is shown in Fig. 2a. The melt in the crucible came out from the inside of the crucible through the holes of the die and the melt (meniscus) spread to the bottom of the die. The meniscus was touched by the $Al_2O_3$ ceramic seed, and a fiber-like eutectic solid was fabricated by pulling down the meniscus. During the fabrication of the undoped STO/TO eutectic solid, the shape of the meniscus was unstable and the diameter of the undoped STO/TO eutectic solid was not constant (Fig. 2b). Figure 2c is a BSE image of the polished surface perpendicular to the growth direction on the undoped STO/TO eutectic solid. There are two phases in the BSE image; however, the phase-separated configuration was not uniform in the eutectic solid, and large grains were observed in addition to the finely separated phases. Then, the insulator configuration was changed to increase the temperature gradient around the liquid–solid interface to stabilize the shape of the meniscus and Nb:STO/TO eutectic solid was grown under the new growth condition. As a result, the shape of the meniscus became constant during fabrication as shown in Fig. 2d; and a Nb:STO/TO eutectic solid with a rectangular column shape could be obtained (Fig. 2e). In the BSE image of the polished surface perpendicular to the growth direction on the Nb:STO/TO eutectic solid, the periodic and uniform eutectic morphology can be observed in Fig. 2d. The

Nb:STO/TO eutectic solid is composed of black phases in a gray matrix phase. Figure 2e is a BSE image of the polished surface parallel to the growth direction on the Nb:STO/TO eutectic solid. There are elongated grains of the black rod-like phase along the growth direction in the gray matrix phase. However, parts of the elongated grains were disordered in the Nb:STO/TO eutectic solid, suggesting that disordering of the black rod phase is attributable to a fluctuation of the liquid–solid interface during the fabrication.

Figure 3a shows the EDX spectra of the black rod and gray matrix phases in the BSE image of the Nb:STO/TO eutectic solid. The EDX spectra reveal that the black rod and the gray matrix phases were TO and STO phases, respectively. Peaks originating from Nb ions were observed in the EDX spectra of both the STO and the TO phases. Actual cation ratios of the STO and TO phases in the Nb:STO/TO eutectic solid were analyzed by the EDX. The actual concentrations of Nd ions in the STO and TO phases were approximately 0.05% and 0.01%, respectively. The powder XRD pattern of the Nb:STO/TO eutectic solid was measured to identify the phases as illustrated in Fig. 3b. All the diffraction peaks in the XRD pattern were indexed as STO with cubic structure (Pm–3m) and TO with tetragonal structure (P42/mnm), demonstrating that the Nb:STO/TO eutectic solid was composed of the two phases of STO and the TO without any impurity phases.

Thermal conductivities, Seebeck coefficients, and electrical resistivities of the Nb:STO/TO eutectic solid parallel and perpendicular to the growth direction are shown in Fig. 4a. The error bars of the thermal conductivity measurements are shown in Fig. 4a, and errors of the Seebeck coefficient and electrical resistivity were less than 0.05%. Thermal
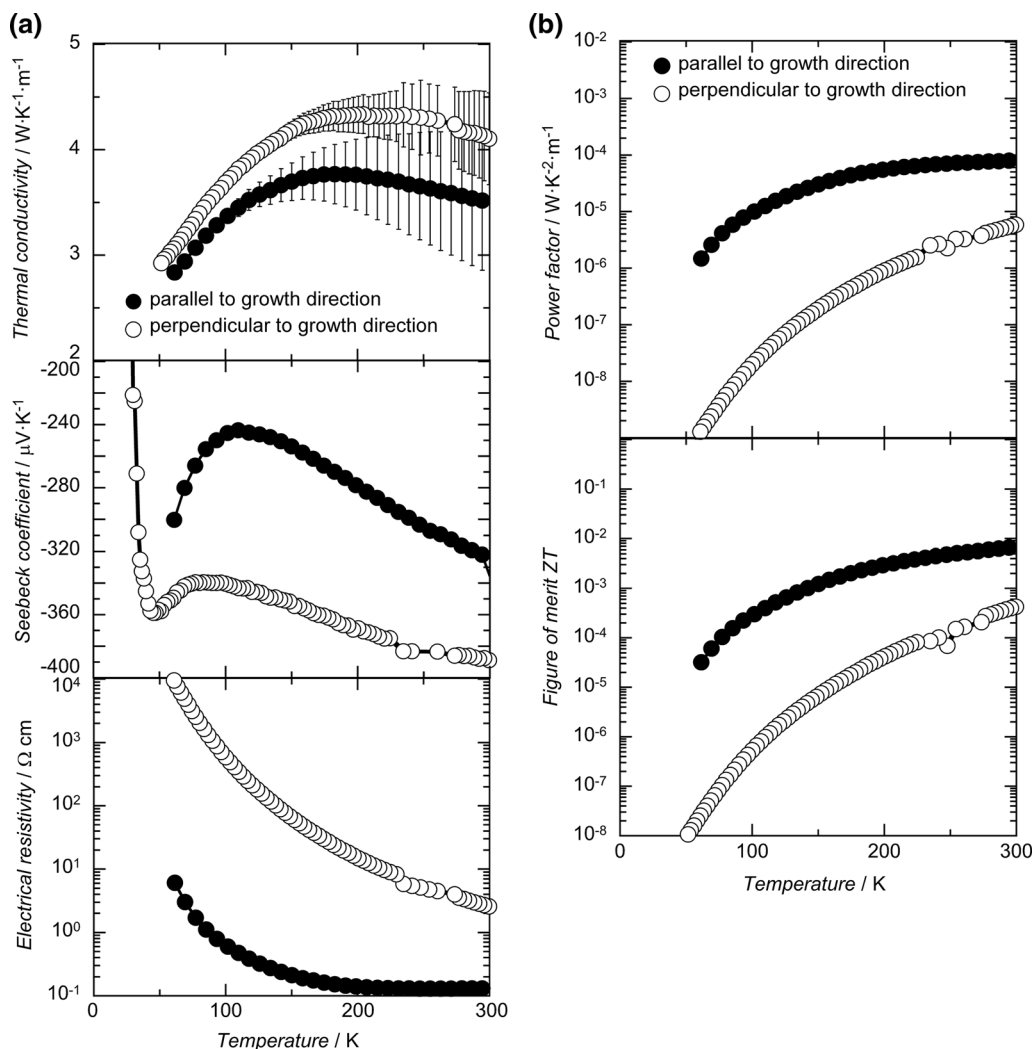
Fig. 4. (a) Thermal conductivities, Seebeck coefficients, and electrical resistivities, and (b) Power factors and figures of merit *ZT* of the Nb:STO/TO eutectic solid.

conductivities at 300 K of the Nb:STO/TO eutectic solid parallel and perpendicular to the growth direction were 3.5 W/(m K) and 4.2 W/(m K), respectively; and these values are less than half of the value of the Nb:STO single crystal at 300 K.[18] This result suggests that the lower thermal conductivity is attributable to a decrease of the lattice thermal conductivity by phonon scattering at the grain boundaries of the eutectic morphology. The Seebeck coefficients of the Nb:STO/TO eutectic solid show similar behavior to that of $(Sr_{1-x}La_x)TiO_3$ [La:STO] single crystals with $x = 0–0.015$.[25] The value of the Seebeck coefficient systematically increased with decreasing temperature in the La:STO with $x > 0.05$. On the other hand, an anomaly at low temperature was observed in the La:STO with $x = 0$ and 0.015 because of the phonon drag effect; and the Nb:STO/TO eutectic solids also indicated the peak at low temperature in Fig. 4a. The temperatures at which the anomalies occurred in the Nb:STO/TO eutectic solids were slightly different from that of the La:STO and the difference of the measurement

direction changed the peak temperature. The mechanism is not clearly understood at the present time; however, these results suggest that the anomaly at low temperature in the Nb:STO/TO eutectic solids is due to the phonon drag effect and that the eutectic structure is affecting the phonon drag effect. The Nb:STO/TO eutectic solids showed much higher electrical resistivities than the Nb:STO single crystal with the doping level of $1.6 \times 10^{20}$ cm$^{-3}$,[18] suggesting that the carrier doping by Nd ions on the STO phase ion was insufficient. As a result, the $ZT$'s of the Nb:STO/TO eutectic solid parallel and perpendicular to the growth direction were $\sim 0.07$ and $\sim 0.0004$, respectively; and they were lower than that of the Nb:STO single crystal because of the higher electrical resistivity.

## CONCLUSIONS

Undoped and Nb-doped STO/TO eutectic solids were fabricated by the $\mu$-PD method. The undoped and Nb-doped (Nb:STO/TO) eutectic solids were

composed of the STO matrix and TO rod phases. The thermal conductivity of the Nb:STO/TO eutectic solid was lower than that of the Nb:STO single crystal owing to the decrease of the lattice thermal conductivity caused by phonon scattering at the grain boundaries. On the other hand, the *ZT* of the Nb:STO/TO eutectic solid was lower than that of the Nb:STO single crystal because of the higher electrical resistivity originating from the insufficient carrier doping level and the high electrical resistivity of the TO phase. However, the results revealed that the thermal conductivity could be decreased by the periodic and uniform eutectic morphology, and *ZT* could be improved by suitable carrier doping and selection of a rod phase with low electrical resistivity. Fabrication of thermoelectric eutectic solids by unidirectional solidification has the advantage of allowing the manufacturing to be carried out in a simple, one-step process without any need for nanopowders; and practical bulk samples with uniform eutectic structure can be produced in the future.

## ACKNOWLEDGMENTS

## REFERENCES

1. W. Kurz and D.J. Fisher, *Fundamentals of Solidification* (London: Trans Tech Publications, 1986).
2. A. Yoshikawa, B.M. Epelbaum, K. Hasegawa, S.D. Durbin, and T. Fukuda, *J. Cryst. Growth* 205, 305 (1999).
3. J.H. Lee, A. Yoshikawa, H. Kaiden, K. Lebbou, T. Fukuda, D.H. Yoon, and Y. Waku, *J. Cryst. Growth* 231, 179 (2001).
4. B.M. Epelbaum, A. Yoshikawa, K. Shimamura, T. Fukuda, K. Suzuki, and Y. Waku, *J. Cryst. Growth* 198–199, 471 (1999).
5. N. Yasui, Y. Ohashi, T. Kobayashi, and T. Den, *Adv. Mater.* 24, 5464 (2012).
6. Y. Ohashi, N. Yasui, Y. Yokota, A. Yoshikawa, and T. Den, *Appl. Phys. Lett.* 102, 051907 (2013).
7. Y. Yokota, S. Kurosawa, K. Nishimoto, V. Chani, and A. Yoshikawa, *J. Eur. Ceram. Soc.* 34, 2095 (2014).
8. K. Nishimoto, Y. Yokota, S. Kurosawa, Y. Fujimoto, N. Kawaguchi, K. Fukuda, and A. Yoshikawa, *J. Eur. Ceram. Soc.* 34, 2117 (2014).
9. T. Mah and T.A. Parthasarathy, *Ceram. Eng. Sci. Proc.* 11, 1617 (1990).
10. M. Yoshimura, S. Sakata, S. Yamada, T. Taishi, and K. Hoshikawa, *J. Cryst. Growth* 427, 16 (2015).
11. B. Zhang, J. Wang, T. Zou, S. Zhang, X. Yaer, N. Ding, C. Liu, L. Miao, Y. Li, and Y. Wu, *J. Mater. Chem. C* 3, 11406 (2015).
12. N. Wang, H. Chen, H. He, W. Norimatsu, M. Kusunoki, and K. Koumoto, *Sci. Rep.* 3, 3449 (2013).
13. F. Maglia, I.G. Tredici, and U. Anselmi-Tamburini, *J. Eur. Ceram. Soc.* 33, 1045 (2013).
14. T. Zhang, Q. Zhang, J. Jiang, Z. Xiong, J. Chen, Y. Zhang, W. Li, and G. Xu, *Appl. Phys. Lett.* 98, 022104 (2011).
15. G. Carotenuto, C.L. Hison, F. Capezzuto, M. Palomba, P. Perlo, and P. Conte, *J. Nanopart. Res.* 11, 1729 (2009).
16. J.R. Sootsman, J. He, V.P. Dravid, C.P. Li, C. Uher, and M.G. Kanatzidis, *J. Appl. Phys.* 105, 083718 (2009).
17. Y. Zhang, L. Wu, J. Zhang, J. Xing, and J. Luo, *Acta Mater.* 111, 202 (2016).
18. S. Ohta, T. Nomura, H. Ohta, and K. Koumoto, *J. Appl. Phys.* 97, 034106 (2005).
19. E.M. Levin, C.R. Robbins, and H.F. McMurdie, *Phase Diagrams for Ceramists* (Columbus: The American Ceramic Society, 1964).
20. Y. Yokota, T. Nihei, K. Tanaka, K. Sakairi, V. Chani, Y. Ohashi, S. Kurosawa, K. Kamada, and A. Yoshikawa, *Adv. Eng. Mater.* 20, 1700506 (2018).
21. Y. Yokota, S. Kurosawa, Y. Shoji, Y. Ohashi, K. Kamada, and A. Yoshikawa, *Opt. Mater.* 65, 46 (2017).
22. T. Kudo, Y. Yokota, M. Sato, K. Tota, K. Onodera, S. Kurosawa, K. Kamada, and A. Yoshikawa, *J. Cryst. Growth* 401, 173 (2014).
23. Y. Yokota, Y. Fujimoto, T. Yanagida, H. Takahashi, M. Yonetani, K. Hayashi, I. Park, N. Kawaguchi, K. Fukuda, A. Yamaji, Y. Fukazawa, M. Nikl, and A. Yoshikawa, *Cryst. Growth Des.* 11, 4775 (2011).
24. Y. Yokota, V. Chani, M. Sato, K. Tota, K. Onodera, T. Yanagida, and A. Yoshikawa, *J. Cryst. Growth* 318, 983 (2011).
25. T. Okuda, K. Nakanishi, S. Miyasaka, and Y. Tokura, *Phys. Rev. B* 63, 113104 (2001).